

Hierarchy-Boosted Funnel Learning for Identifying Semiconductors with Ultralow Lattice Thermal Conductivity

Mengfan Wu,^{1,2} Shenshen Yan,² and Jie Ren^{1,2,*}

¹Shanghai Research Institute for Intelligent Autonomous Systems, Tongji University, Shanghai 200092, China

²Center for Phononics and Thermal Energy Science, Shanghai Key Laboratory of Special Artificial Microstructure Materials and Technology, School of Physics Science and Engineering, Tongji University, Shanghai 200092, China

(Dated: January 14, 2025)

Data-driven machine learning (ML) has demonstrated tremendous potential in material property predictions. However, the scarcity of materials data with costly property labels in the vast chemical space presents a significant challenge for ML in efficiently predicting properties and uncovering structure-property relationships. Here, we propose a novel hierarchy-boosted funnel learning (HiBoFL) framework, which is successfully applied to identify semiconductors with ultralow lattice thermal conductivity (κ_L). By training on only a few hundred materials targeted by unsupervised learning from a pool of hundreds of thousands, we achieve efficient and interpretable supervised predictions of ultralow κ_L , thereby circumventing large-scale brute-force calculations without clear objectives. As a result, we provide a list of candidates with ultralow κ_L for potential thermoelectric applications and discover a new factor that significantly influences structural anharmonicity. This study offers a novel practical pathway for accelerating the discovery of functional materials.

I. INTRODUCTION

Emerging as a powerful technology of the data-driven paradigm in materials science, machine learning (ML) has considerably accelerated the design and discovery of promising materials in recent years,[1–4] including ML interatomic potentials,[5] inverse design of materials,[6] efficient property predictions.[7, 8] Simultaneously, the advancements in high-performance computing greatly facilitate the establishment of diverse material-related databases utilizing density functional theory (DFT)-based high-throughput calculations (HTC), such as the Materials Project (MP),[9] Open Quantum Materials Database (OQMD),[10, 11] Automatic-FLOW for Materials Discovery (AFLOW),[12] Joint Automated Repository for Various Integrated Simulations (JARVIS),[13] etc. These continuously expanding databases also lay a solid foundation for the application of cutting-edge ML technology in the field of materials science.

As the two main categories of ML, namely supervised and unsupervised learning strategies, both have achieved remarkable success in different ways. On the one hand, supervised learning enables the efficient predictions of material properties by-passing solving the complex equations of quantum mechanics based on expensive DFT calculations, which emphasizes the requirement of large human-labelled datasets for model training to ensure the accuracy. Ridge regression,[14] decision tree,[15] support vector machine,[16] random forest,[17] gradient boosting decision tree,[18] etc., are widely employed in designing and screening potential materials with desired properties, which also elucidate the close relationship between the structure and target property.[19–21] On the other hand, as a technology operates without the necessity of well-labeled training data, unsupervised learning possesses the capability to infer the underlying patterns among

varieties of materials within a feature space. Predominantly employed methods in unsupervised learning encompass clustering, dimensionality reduction, and anomaly detection, in which clustering can categorize different materials into the corresponding clusters by assessing their similarities between each other, thereby identifying candidates resembling the anticipated data points.[22–24] In this context, combining HTC and ML technologies can not only efficiently explore novel materials in the vast chemical space but also gain insights into the structure-property relationship at a quantitative level. However, a significant challenge lies in labeling data for materials with intrinsically complex properties in the vast chemical space, especially the lattice thermal conductivity (κ_L), due to the complexities involved in experimental measurements and the unbearable computational costs associated with accurate DFT calculations. Is there an effective approach to reduce the cost of labeling, while enabling the efficient prediction of complex properties and elucidation of structure-property relationships?

Functional materials exhibiting ultralow κ_L possess vital significance across various fields, such as power generation,[25] heat conduction,[26] thermal barrier coatings[27] and so on,[28–30] which greatly advance the development of industry. Particularly, owing to the key role in directly converting heat energy into electricity based on the thermoelectric (TE) effect, TE materials have become the focal point of considerable interest in academic and industrial research. Indeed, the conversion efficiency of a TE material is theoretically quantified by its figure of merit zT : $zT = S^2\sigma T/\kappa$, where S is the Seebeck coefficient, σ is the electric conductivity, κ is the thermal conductivity, and T is the absolute temperature, respectively. Moreover, κ can be expressed in two parts: $\kappa = \kappa_e + \kappa_L$, where κ_e and κ_L are the electronic thermal conductivity and lattice thermal conductivity, respectively, indicating that they all contribute to heat conduction. For metallic materials, κ_e plays a dominant role in heat conduction due to the presence of a large number of free electrons. On the contrary, in semiconductors or insulators, thermal energy is predominantly

* Corresponding author
E-mail: Xonics@tongji.edu.cn

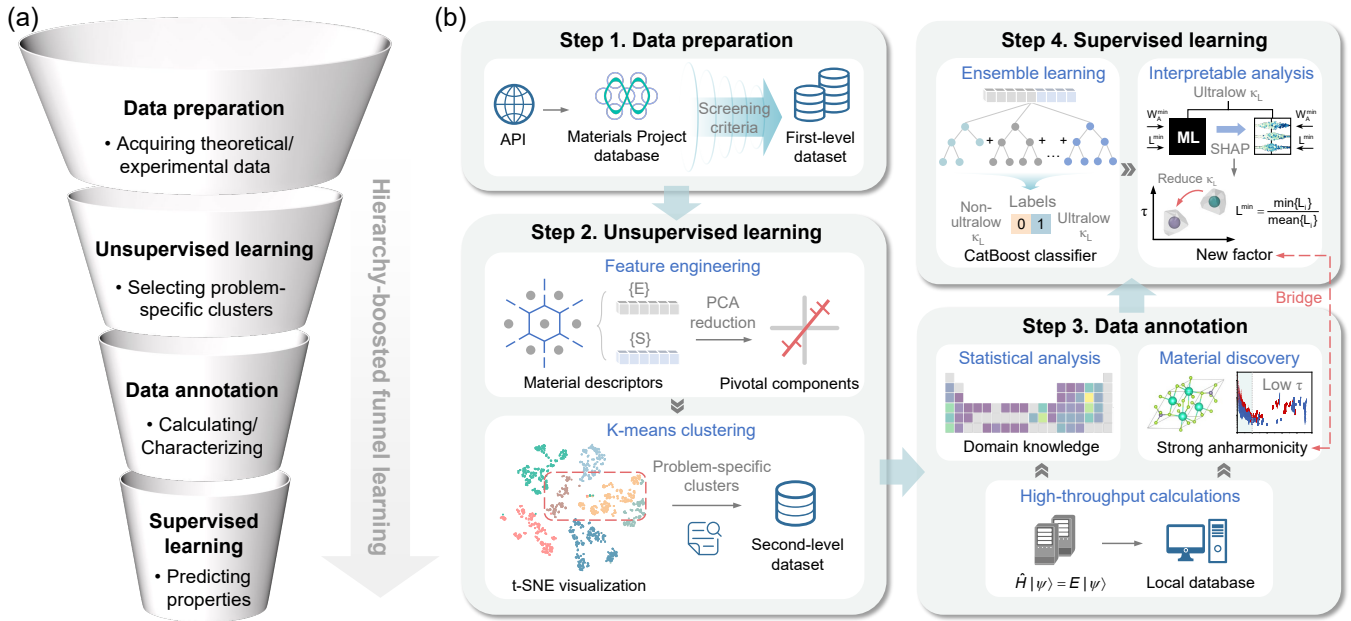


Figure 1. (a) Schematic of the novel HiBoFL framework, including data preparation, unsupervised learning, data annotation and supervised learning. (b) Workflow of applying HiBoFL framework to efficiently identify semiconductors with ultralow κ_L .

transferred through lattice vibrations, with κ_L making the primary contribution. In this process, the quanta of such lattice vibrations in a solid are the so-called phonons.

As clearly noticed, toward the goal of seeking TE materials with optimal zT values, it requires not only maximizing the power factor ($S^2\sigma$) but also minimizing the thermal conductivity ($\kappa_e + \kappa_L$) simultaneously.[31] Notably, the distinct and separate scale of the mean free paths for electrons and phonons contributes to the independence of κ_L as a parameter in zT , which makes decreasing κ_L become a significant avenue to realize the ideal concept of “phonon-glass and electron-crystal”,[32, 33] ultimately leading to excellent TE performance. For the past decades, unremitting efforts have been made to discover a series of materials with κ_L , for instance, Ti_3VSe_4 ,[34] TlInTe_2 ,[35] InTe ,[36] CsAg_5Te_3 ,[37] AgSbSe_2 ,[38] etc. However, the conversion efficiency of TE materials has persistently been a significant challenge in the efficient recovery of waste heat, that is to say, useful materials featuring ultralow κ_L are still in urgent demand. Despite the few successes of traditional trial-and-error experiments and case-by-case DFT calculations in the exploration of desired materials, efficient and robust material design oriented towards κ_L in the vast chemical space is hindered by the complex structure-property relationship and size-limited resources.

In the present work, we propose a novel hierarchy-boosted funnel learning (HiBoFL) framework that integrates unsupervised learning and supervised learning to efficiently achieve complex property predictions, which is applied to identify semiconductors with ultralow κ_L . Unsupervised learning is used to uncover underlying patterns among different materials, facilitating the identification of specific clusters with a high likelihood of exhibiting ultralow κ_L . Based the low-

cost HTC on this significantly reducing space, we establish a local database and discover a series of semiconductors with ultralow κ_L , in which Cs_2SnSe_3 and Cs_2GeSe_3 are screened out for in-depth mechanism analysis. Furthermore, a supervised classification model for directly predicting ultralow κ_L is trained to refine the results. With resolved important descriptors that govern ultralow κ_L , we are capable of investigating the κ_L modulation mechanism and uncovering a new factor that governs structural anharmonicity. We expect that this HiBoFL framework can also be widely applied in the discovery of other functional materials with excellent performances.

II. RESULTS AND DISCUSSION

A. HiBoFL Framework for Accelerating the Discovery of Functional Materials

Our proposed novel HiBoFL framework for accelerating the discovery of functional materials with complex properties is shown in Figure 1a, which exhibits a funnel-like structure driven by a hierarchical framework, effectively narrowing the search space while boosting model performances. This framework mainly includes four parts: I) Data preparation. An initial theoretical or experimental dataset of the target material system is required, potentially involving preliminary high-throughput screening, data cleaning, and other preprocessing operations. II) Unsupervised learning. Relevant features are extracted from the initial dataset, encompassing aspects such as experimental process parameters, intrinsic material properties, etc. By employing clustering algorithms, distinct classes of data points with potentially similar properties can be identi-

fied, in which problem-specific clusters are selected to narrow the search space. III) Data annotation. Data from the problem-specific clusters can be assigned corresponding property labels through further relatively low-cost experimental characterizations or HTC. This facilitates the establishment of a local database, enabling the extraction of prior domain knowledge through statistical data analysis. IV) Supervised learning. The labeled dataset within the established local database can be used to further train supervised learning models, which helps refine the coarse results from unsupervised learning, ultimately enabling direct and rapid prediction of the target properties. Such a HiBoFL framework can not only reduce the expensive cost of labeling data, but also efficiently predict the costly-labeled complex properties.

We then apply this HiBoFL framework to efficiently identify semiconductors with ultralow κ_L as shown in Figure 1b. In the first step, we obtain the material dataset from the MP database based on its application programming interface (API) and then apply a series of screening criteria to derive the first-level dataset for subsequent research. In the second step, chemical composition descriptors based on Magpie[39] and crystal structure descriptors derived from Voronoi tessellations[40] are used to featurize the materials in the first-level dataset. We use principal component analysis (PCA),[41] for dimensionality reduction thereby obtaining pivotal components. K -means clustering is then employed to identify materials with similar κ_L , which is visualized in a low-dimensional space using t-distributed Stochastic Neighbor Embedding (t-SNE),[42] and problem-specific clusters are selected based on similarity design rules to form the second-level dataset. In the third step, we use the phonon-elasticity-thermal (PET) model[43] to perform low-cost HTC on the materials in the second-level dataset, establishing a local database based on the HTC results. On the one hand, a list of candidates for potential TE applications can be recommended and their statistical analysis can help us to summarize several domain knowledge of ultralow κ_L . On the other hand, we can directly screen out candidate materials with ultralow κ_L for in-depth mechanism analysis, where the results are verified by accurately solving the Boltzmann transport equation and the phonon thermal transport mechanisms are further revealed. In the fourth step, we perform ensemble learning on the labeled local database for directly classifying ultralow κ_L , training a robust CatBoost classifier[44]. The interpretable analysis of the pre-trained model based on the SHapley Additive exPlanations (SHAP) method[45, 46] further reveals the influence of important descriptors on ultralow κ_L . A new factor capable of significantly reducing κ_L via enhancing structural anharmonicity is discovered, eventually building a bridge between the ML model interpretability and first-principles analysis.

B. Preliminary High-Throughput Screening

The process of preliminary high-throughput screening to select materials for subsequent ML investigations is illustrated in Figure 2a. Initially, we start by acquiring all the materials

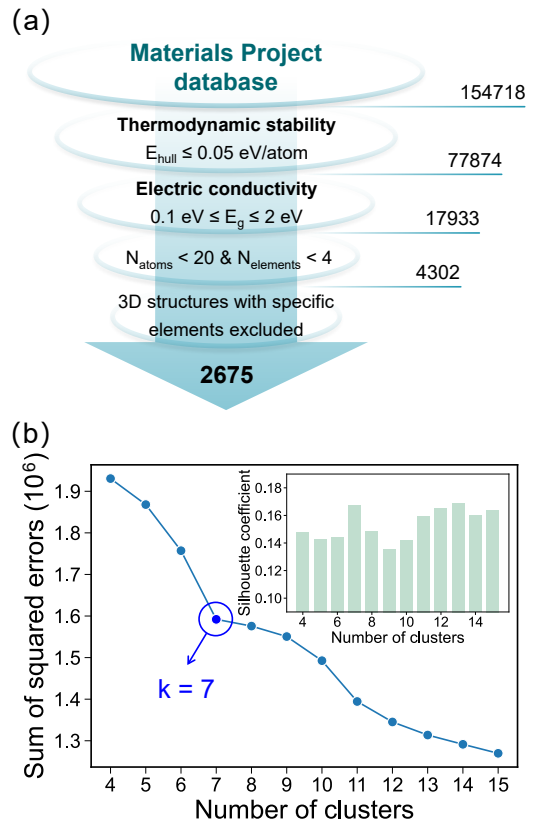


Figure 2. (a) Flowchart of preliminary high-throughput screening from the Materials Project (MP) database. (b) Optimization of the number of clusters k for the k -means algorithm based on the elbow method and silhouette coefficient (inset).

from the MP database based on its API, resulting in a total of 154718 entries saved in a JSON file as the Python dictionary object. Of these, several specific criteria are set to narrow down the range of exploration. The first screening criterion focuses on the assessment of thermodynamic stability, in which the materials with energy above the convex hull (E_{hull} , the formation energy difference between the target compound and its competing phases) no more than 0.05 eV/atom are considered to show a high likelihood of being synthesized in experiment. Further, the band gap (E_g) can be directly retrieved from the MP database, set within the range of 0.1–2 eV for assessing electric conductivity. This specific interval is highly characteristic of semiconductors, demonstrating the inherent capacity of these screened materials for favorable electrical conductivity. Additionally, taking into account of the computational cost associated with κ_L , our constraints on the material system involve ensuring that the number of atoms (N_{atoms}) is less than 20 in the unit cell of a crystal structure and the number of elements (N_{elements}) is below four in one compound, respectively. Ultimately, through excluding the materials containing hydrogen, lanthanides, and actinides, and conducting structural analysis, we further obtain 2675 three-dimensional (3D) crystal structures without calculation errors. These materials

constitute the first-level dataset for our in-depth investigations.

C. Unsupervised Learning for Identifying Materials with Similar κ_L

We next carry out unsupervised learning to identify materials with a high likelihood of exhibiting relatively low κ_L based on similarity design rules. Following the generation of the first-level dataset as input, the materials should be transformed into the length-fixed vector as the so-called descriptors, which are the key point to distinguish different materials. Herein, we use two distinct types of descriptors to featurize these materials, namely, composition-based features and structure-based features, to account for the mapping relationships between different categories of descriptors and κ_L from the perspectives of chemical composition and crystal structure. Among them, composition-based features are generated based on Magpie data and denoted by $\{E\}$, including electronegativity, atomic number, fraction of electrons, etc., which are comprehensive enough to capture the characteristics of chemical compositions with different constituent elements and proportions. Through partitioning the crystal structures into Wigner-Seitz cells of each atom, a series of structure-based features can be derived from Voronoi tessellations based on the characteristics of local environment of each atom in the unit cell, which are denoted by $\{S\}$. In this manner, each material can generate a total of 273 descriptors automatically without any time-consuming DFT calculations based on its corresponding composition and structure, jointly denoted by $\{E, S\}$. Notably, these descriptors have been successfully applied to the ML predictions of κ_L at various temperatures, indicating their significant potential for mapping the property of κ_L . After feature generation, it is crucial to preprocess all the data thereby enhancing the performance of clustering model. To address the large variations among different feature values and transform them to follow a normal distribution, both standardization and Quantile Transformer are employed for preprocessing these descriptors. Further, we perform PCA based on Singular Value Decomposition to project the preprocessed features to a lower dimensional space. PCA linearly combines original features into principal components (PCs), ensuring the hierarchical order based on their contributions, in which the first principal component captures the largest explainable variance, followed by the second one and so forth. From the curve of total explainable variance changing with the number of PCs as shown in Figure S1, we can conclude that 83 PCs suffice to account for 99% of the variance among all 2675 materials in the first-level dataset. Hence, these 83 PCs are extracted as the pivotal components for input into the following clustering algorithm.

Subsequently, the k -means algorithm is utilized to identify the underlying associations with κ_L from these unlabeled materials, in which only one critical parameter is required to be predefined, i.e., the number of clusters k . Based on the analysis of the elbow method[47] and the silhouette coefficient[48] as depicted in Figure 2b, the elbow-like point of inflection on the curve emerges at a value of $k = 7$, indicating the loca-

tion where inertia or distortion start decreasing significantly with a very slow rate, represents the optimal k value for the k -means clustering. At this stage, a relatively high silhouette coefficient also illustrate that each material exhibits strong similarity within its respective cluster, while different clusters are well-separated as much as possible. As a result, we partition the first-level dataset into seven clusters (from C_1, C_2, \dots , to C_7), on the basis of similarities of these feature vectors derived from chemical compositions and crystal structures, in which the materials in the same cluster are considered to show a high likelihood of possessing similar κ_L . Since the first two PCs only capture about 35% of the variance within entire data, it is insufficient for the clustering results to be intuitively visualized in a two-dimensional (2D) mapping. Unlike PCA, which emphasizes preserving large pairwise distances to maximize variance, t-SNE is a powerful non-linear dimensionality reduction technology for the visualization of high-dimensional data, aiming to maintain pairwise similarities among data points in a lower-dimensional space. We strictly use t-SNE only for the visualization of the resulting seven clusters of k -means algorithm as shown in Figure 3, projecting the 83 PCs into a 2D latent space comprised of two t-SNE components. The result intuitively demonstrates the high-quality clustering with distinct separation between each cluster, where each point represents a material and its color relates to the corresponding category of cluster.

Since we have obtained seven clusters through k -means clustering, it is necessary to conduct the similarity analysis of these clusters. Materials within the same cluster are considered to show similar structures thereby likely sharing similar properties, which facilitates a deep comprehension of underlying patterns and relationships among the 2675 materials. To evaluate the similarity criteria of these materials, the reported κ_L values at 300 K for several known materials included in each cluster are collected from the previous studies (most are experimentally measured), which are all listed in Table S1 along with some other basic information. As we expected, materials within the same cluster exhibit closely similar κ_L values, while there is a comparatively significant difference in κ_L among materials from different clusters. Particularly, the known materials with relatively low κ_L are clustered into C_1 and C_2 through k -means clustering, including eight structures of Ti_3AsSe_3 (0.23 W/mK),[49] Ti_2Te_3 (0.40 W/mK),[50] Ti_3SbS_3 (0.42 W/mK),[51] TiBiS_2 (0.80 W/mK),[52] CuBr (1.30 W/mK),[53] Cu_2GeS_3 (1.20 W/mK),[50] RbSbS_2 (1.60 W/mK)[51] and AgGaS_2 (1.50 W/mK),[54] which are all clearly shown in the enlarged part of Figure 3. On the contrary, C_7 contains materials with apparently large κ_L , including four structures of GaN (130 W/mK),[55] BP (350 W/mK),[56, 57] SiC (490 W/mK)[58] and Si (156 W/mK).[59] Thus, as confirmed by the good distinction between low and high κ_L among each cluster, our proposed unsupervised learning model demonstrates great potential to identify compositional and structural information about the κ_L of these materials, leading to the successful clustering into different categories according to this property. Since the materials with a high likelihood of possessing relatively low κ_L tend to group into the two clusters of C_1 and C_2 , the expo-

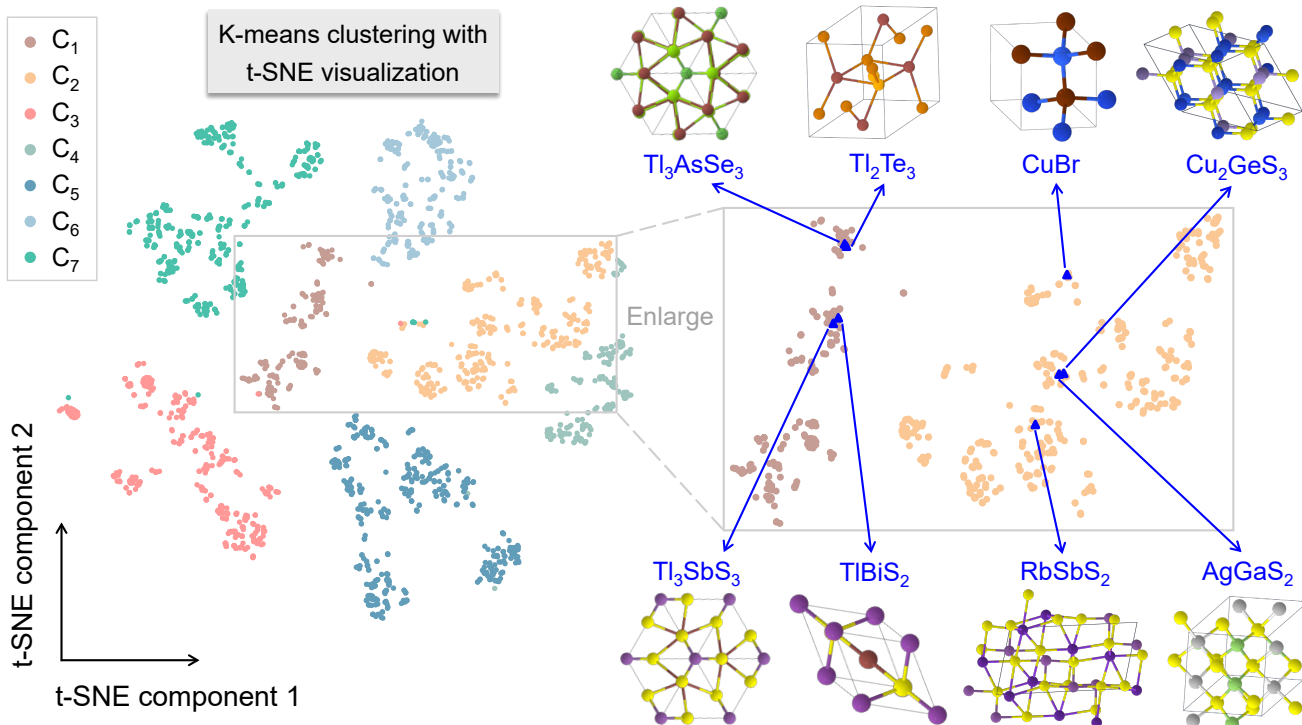


Figure 3. Unsupervised learning of the materials in the first-level dataset. Using t-SNE visualization for the seven clusters generated by the k -means algorithm, where each point represents a compound and is colored with the corresponding cluster. Eight represented materials in C_1 and C_2 with low experiment-measured κ_L are marked in the enlarged region.

ration scope for finding materials with low κ_L is reduced from 2675 materials to 704 materials, narrowing by approximately three-quarters. As a result, these two problem-specific clusters (C_1 and C_2) further constitute our second-level dataset.

D. HTC of Specific Clusters and Statistical Analysis

Given the success of unsupervised learning in significantly reducing the broad material search space, it has become feasible to further extend the second-level dataset into a labeled repository of thermal conductivity through HTC at affordable computational costs. Based on the PET empirical equation within the high-throughput framework, we derive the κ_{PET} values at 300 K ignoring the anisotropy for materials in the second-level dataset, while excluding structures that do not satisfy the mechanical stability criteria. The basic information and corresponding κ_{PET} values of the resulting 661 materials are then stored in a local database using MongoDB,[60] serving as a valuable repository for researchers to retrieve data and prioritize detailed theoretical and experimental investigations. Of particular note is that nearly 70% of these semiconductors exhibit the κ_{PET} values no greater than 2 W/mK (Figure 4a), with a considerable portion of these materials remaining unreported to date. These materials also constitute a list of candidate materials with potential applications in the TE field, which undoubtedly prove that the specific clusters

we identified through unsupervised learning indeed contain a significant number of materials with low thermal conductivity.

In addition, we also count the distribution of different formula types with counts exceeding 20 in these materials. Apparently, the structures represented by the two types of formula anonymous dominate in quantity, namely the ABC_2 type characterized by the diamond-like structure, and the ABC_3 type represented by the perovskite-type structure. To gain a more intuitive insight into the distribution patterns of materials with low thermal conductivity, we plot a heat map over the periodic table of elements in Figure 4b, illustrating the count of elements present in these compounds with κ_{PET} no greater than 2 W/mK. Sulfur, selenium, tellurium, and oxygen belonging to the chalcogens consecutively occupy the largest counts among the anion elements, in which sulfur is the most abundant with a count of 102. As for the cation elements, silver, cesium, potassium, copper, and rubidium occupy the highest abundance respectively. This can be explained by the fact that materials composed of heavy elements or characterized by weak chemical bonding typically exhibit lower κ_L . Notably, a few previous studies have constrained the search space of materials within the above-mentioned characteristics to investigate those with low thermal conductivity, such as high-throughput screening in chalcogenide ABC_3 perovskites[61] or diamond-like ABC_2 compounds,[62] detailed analysis in the IV–VI chalcogenides[63] and so forth.[38, 64–66] The box plot of different crystal systems indicates that the κ_{PET} values of ma-

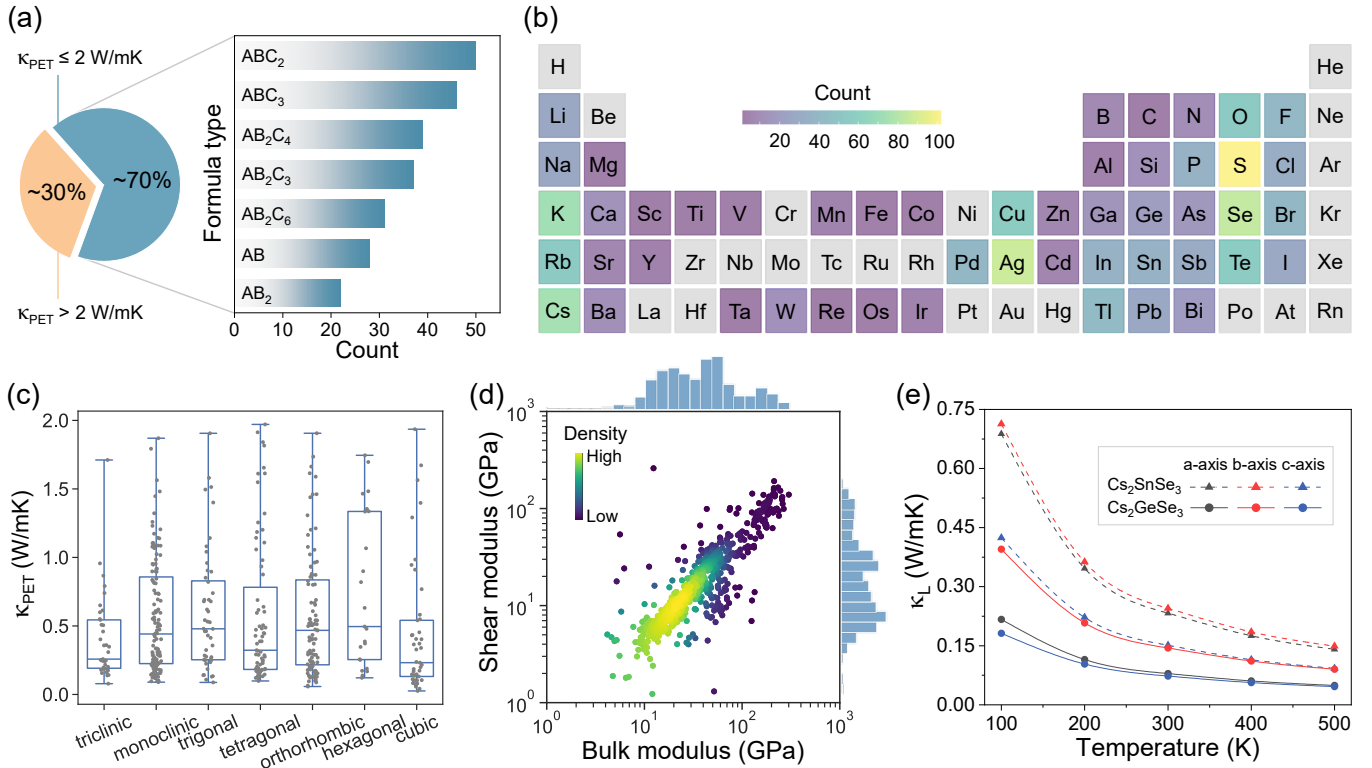


Figure 4. (a–d) Statistical analysis of HTC results in the second-level dataset. (a) Pie chart of κ_{PET} separated by a threshold of 2 W/mK and distribution of different formula types with counts exceeding 20. (b–d) Distribution of the materials with κ_{PET} no greater than 2 W/mK: (b) Heat map over the periodic table of elements for easy visualization of element counts. (c) Box plot of different crystal systems. (d) Density scatter plot of shear modulus and bulk modulus. (e) Calculated κ_{L} as the function of temperature at different axes in Cs_2SnSe_3 and Cs_2GeSe_3 by solving the phonon Boltzmann transport equation.

materials in each crystal system primarily cluster around 0.5 W/mK, with the monoclinic system exhibiting the largest quantity (Figure 4c). We also show the density distributions of the shear modulus and bulk modulus obtained by the Voigt–Reuss–Hill (VRH) method as shown in Figure 4d, which are primarily concentrated within the relatively small range of ~ 50 GPa. This suggests that materials with lower shear and bulk moduli might be more likely to exhibit lower thermal conductivity. These statistical analyses provide deep insights into the regulation of κ_{L} , which can offer prior domain knowledge for researchers in selecting specific systems to obtain ultralow κ_{L} .

To further validate the results and conduct in-depth analysis of the phonon thermal transport mechanism, we calculate more precise κ_{L} values according to first-principles derived force constants and Boltzmann transport theory for the unreported materials Cs_2SnSe_3 and Cs_2GeSe_3 , which are screened out based on the formula type ranking among the materials with the lowest κ_{PET} values. Figure 4e depicts the calculated κ_{L} as the function of temperature ranging from 100 to 500 K at different axes in the discussed semiconductors, in which all the intrinsic κ_{L} values show obvious anisotropy and gradually decrease following the T^{-1} manner with the temperature increasing just as the hallmark of Umklapp scattering. The rise in temperature results in an elevation in the equilibrium

phonon population, consequently leading to intense phonon-phonon collisions, as delineated by $\bar{n} \approx k_{\text{B}}T/\hbar\omega$ ($T \gg \Theta_{\text{D}}$), where \bar{n} is the average number of phonons, k_{B} is the Boltzmann constant, T is the temperature, ω is the frequency, \hbar is the reduced Planck constant and Θ_{D} is the Debye temperature. Moreover, these materials all exhibit intrinsically ultralow κ_{L} , with values all below 0.25 W/mK in any direction at 300 K, significantly lower than the κ_{L} (~ 2.3 W/mK) of the traditional TE material PbTe.[67] The results indicate the potential application of Cs_2SnSe_3 and Cs_2GeSe_3 in the TE field, further substantiating the effectiveness of our previously adopted approach—combining unsupervised learning with HTC to discover semiconductors with ultralow κ_{L} .

E. Mechanisms of Phonon Thermal Transport Properties

Generally speaking, compounds with heavier atoms tend to exhibit lower group velocities due to the reduced phonon frequency. As a result, a lower κ_{L} of Cs_2SnSe_3 was expected given the relatively heavy nature of Sn. However, it is noteworthy that the κ_{L} of Cs_2SnSe_3 is obviously higher than that of Cs_2GeSe_3 (i.e., ~ 3 times in the a -axis, ~ 1.7 times in the b -axis, ~ 2 times in the c -axis at 300 K), which presents an interesting unusual phenomenon. Next, we would like to dis-

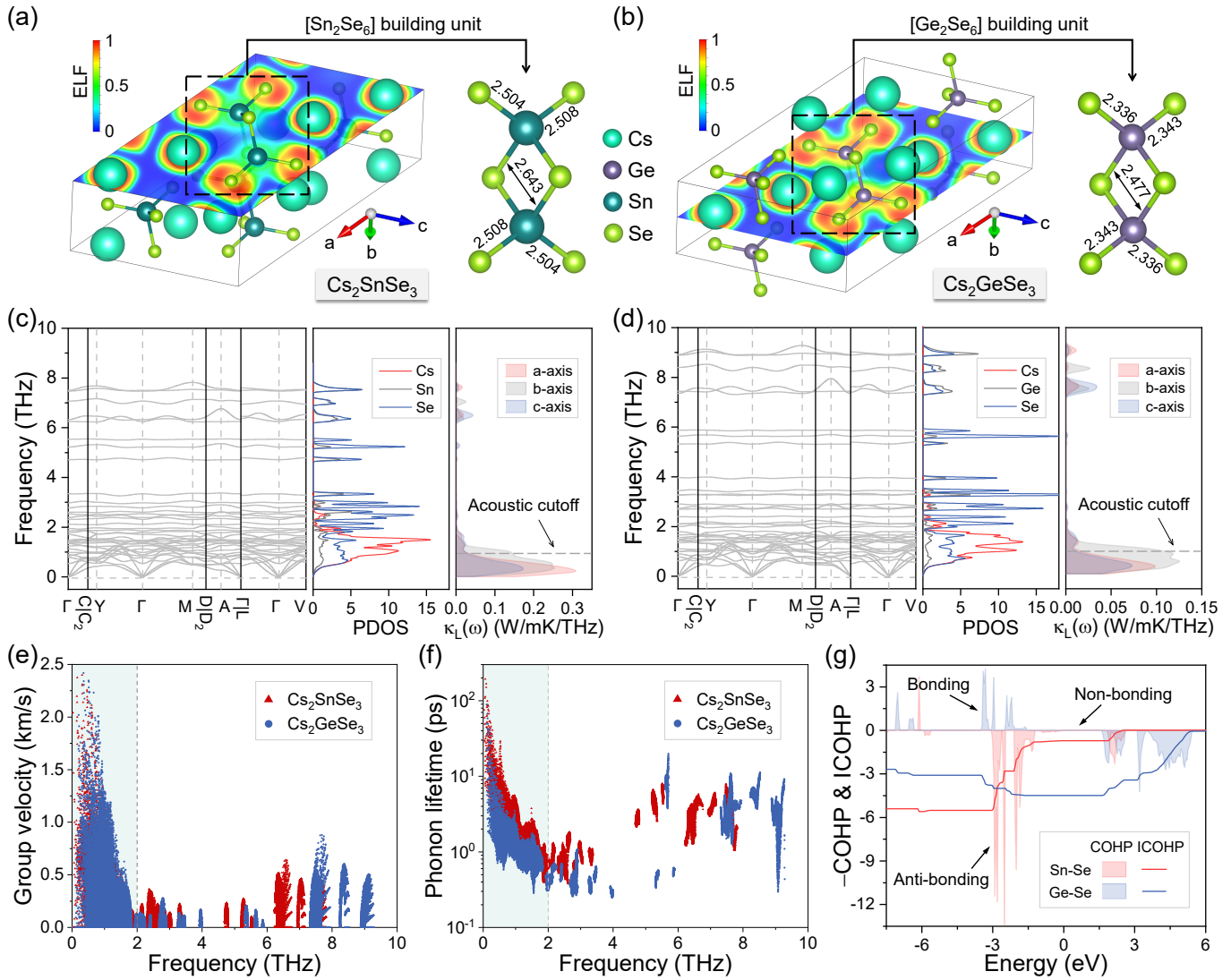


Figure 5. (a–g) First-principles analysis of the phonon thermal transport properties. Crystal structures and the projected 2D ELF diagram of (a) Cs_2SnSe_3 and (b) Cs_2GeSe_3 . Phonon dispersion (left panels), atom-projected PDOS (middle panels) and spectral $\kappa_L(\omega)$ (right panels) of (c) Cs_2SnSe_3 and (d) Cs_2GeSe_3 . (e) Group velocity along the b -axis and (f) phonon lifetime as a function of frequency at 300 K for Cs_2SnSe_3 and Cs_2GeSe_3 . (g) COHP and ICOHP projected on Sn–Se and Ge–Se bonds.

discuss the microscopic mechanisms responsible for the ultralow κ_L and unusual difference observed among the two materials.

Cs_2SnSe_3 and Cs_2GeSe_3 both crystallize in the same space group $C2/m$ (No. 12) of the monoclinic crystal system, with the fully optimized crystallographic parameters listed in Table S2. Their crystal structures are shown in Figures 5a and 5b. Sn/Ge atoms are coordinated by four Se atoms in a tetrahedral geometry $[\text{SnSe}_4]/[\text{GeSe}_4]$ at distances in 2.504–2.643 Å/2.336–2.477 Å, and these tetrahedra further share a common edge to form dimeric $[\text{Sn}_2\text{Se}_6]/[\text{Ge}_2\text{Se}_6]$ building units, respectively, which form the four-membered $[\text{Sn}_2\text{Se}_2]/[\text{Ge}_2\text{Se}_2]$ rings and are charge compensated by Cs cations. The phase diagrams for Cs–Sn–Se and Cs–Ge–Se systems based on the calculated energies in the MP database show that Cs_2SnSe_3 and Cs_2GeSe_3 possess similar thermodynamical stability with equal (zero) convex hull distances

(Figure S2). Simultaneously, the phonon dispersion curves along high-symmetry directions in Brillouin zone indicate that they are dynamically stable due to the absence of imaginary phonon modes (left panels in Figures 5c and 5d). Thus, the results demonstrate the feasibility of experimentally synthesizing these two materials. To identify the bonding characteristics in Cs_2SnSe_3 and Cs_2GeSe_3 , we employ the electron localization function (ELF) to quantify the extent of spatial localization of the reference electron with values ranging from 0 to 1. The localization of electrons in the Sn/Ge–Se bonding region illustrates the covalent nature of the Sn/Ge–Se bonds, in which a polar covalent bond between Sn and Se (ELF \approx 0.5) is observed due to the smaller electronegativity and larger atomic radius of Sn, leading to a significant difference among the two compounds. On the contrary, there is no overlapping of charge clouds between Cs atoms and other atoms, indicat-

ing the presence of strong ionic bonding which aligns with the fact that a relatively large electronegativity (on the Pauling scale) difference (1.76) between Cs (0.79) and Se (2.55) results in strong ionic characteristics. Therefore, Cs_2SnSe_3 and Cs_2GeSe_3 contain multiple types of bonds, i.e., ionic Cs–Se and covalent Sn/Ge–Se, resulting in complex crystal structures with bonding hierarchy. These complex structures, comprising heavy atoms, weakly bound and rigid distorted units with a significant bonding hierarchy, are anticipated to exhibit large lattice anharmonicity.[68]

The phonon dispersion reveals that there are 3 acoustic branches and 33 optical branches at each phonon wave vector q due to the 12 atoms in the primitive cell of both Cs_2SnSe_3 and Cs_2GeSe_3 , in which three acoustic branches are composed of one longitudinal acoustic mode (LA) and two transverse acoustic modes (TA and TA'). A striking common feature of their phonon dispersion is that a waterfall-like low-lying optical branch (LLO) exhibits the avoided crossing behavior with acoustic modes around the Brillouin zone center, resulting in strong acoustic-optical coupling as one of the potential signals of the rattling model.[69] These characteristics can not only lead to a softening of the acoustic modes thereby yielding low phonon group velocities, but also greatly enhance the scattering rates of heat-carrying acoustic phonons, all of which contribute to the suppression of κ_L for Cs_2SnSe_3 and Cs_2GeSe_3 . Analysis of the atom-projected PDOS and spectral $\kappa_L(\omega)$ (middle and right panels in Figures 5c and 5d) indicate that acoustic and LLO phonon modes in the low-frequency range (0–2 THz) are primarily dictated by Cs and Se vibrations followed by Sn/Ge vibrations, which also make predominant contributions to the ultralow κ_L . A localized region mostly contributed by Cs atoms within a narrow energy window centered around 1 THz is observed in both compounds, indicating the anharmonic rattling-like motion of the weakly bonded Cs atoms, which is responsible for the presence of the soft LLO modes. This can also be confirmed in the potential energy curves obtained by shifting the atoms with respect to their static equilibrium positions along different axes as depicted in Figure S3. Sn/Ge and Se atoms are both confined within the comparatively steep potential wells, whereas Cs atoms with heavier mass can vibrate easily with larger amplitude due to the shallowest potential energy surface in all the direction. These atoms exhibit nearly identical displacement magnitudes in their respective compounds. Therefore, the loosely bound Cs atoms are surrounded by $[\text{Sn}_2\text{Se}_6]/[\text{Ge}_2\text{Se}_6]$ units thereby exhibiting the same rattling-like effect, which can result in a common strong anharmonicity in both compounds.[70, 71]

Figures 5e and S4 show the frequency dependence of the group velocity v from all the q points in different axes at 300 K for Cs_2SnSe_3 and Cs_2GeSe_3 , as given by $v_\lambda = \partial\omega_\lambda/\partial q$. Most of the phonon modes possess ultralow v values less than 2 km/s, confirming the lattice softening induced by the weak interatomic bonding, which is also consistent with the flat phonon bands observed in the phonon dispersion. Figure 5f depicts the overall short τ values mainly ranging from 0.2 ps to 20 ps, with low-frequency phonons exhibiting a gradual shortening trend in both compounds. This can be attributed

to the presence of LLO modes, which facilitates more scattering paths and impedes the heat flow, significantly enhancing the scattering rates thereby reducing τ for both acoustic and LLO modes, ultimately reducing κ_L . It is noteworthy that in the low-frequency phonon region, particularly within the acoustic phonon range, the phonon group velocities of these two compounds show little difference, yet the phonon lifetime of Cs_2SnSe_3 is significantly longer than that of Cs_2GeSe_3 . Therefore, we conclude that the relatively lower anomalous κ_L of Cs_2GeSe_3 is attributed to its shorter phonon lifetime.

We speculate that the difference in the phonon lifetime between Cs_2SnSe_3 and Cs_2GeSe_3 might be related to the strength of Sn–Se and Ge–Se covalent bonding. This covalent bonding may induce anisotropic motion, involving the collective movement of Sn/Ge and Se atoms, thereby leading to a strong lattice anharmonicity within the system.[72] To support this conclusion, we perform crystal orbital Hamilton population (COHP) calculations[73] to identify the energy-resolved local bonding information. Figure 5g shows that antibonding states persist down to -3 eV below the Fermi level (E_F) in Sn–Se bonding, which can weaken the corresponding bonding strength thereby forming a polar covalent bond as observed in ELF. This can be demonstrated by the integral of COHP (ICOHP = $\int_{-\infty}^E \text{COHP}(E)dE$) at the E_F , which represents all occupied orbitals, serving as an indicator of bond strength. Since the average ICOHP values for Sn–Se and Ge–Se bonds are -0.72 eV and -4.49 eV, respectively, indicating the obvious weaker Sn–Se bonding in Cs_2SnSe_3 . The stronger bonding strength of Ge–Se is also evident from its larger force constant $|\Phi_{ij}|$ in comparison to that of Sn–Se (Figure S5). Hence, the shorter phonon lifetime of Cs_2GeSe_3 relative to Cs_2SnSe_3 may be attributed to their significant difference in Ge–Se and Sn–Se covalent bonding, which can be further quantified at the structural descriptor level through subsequent interpretable ML approaches.

F. Interpretable Supervised Classification for Predicting Ultralow κ_L

After labeling the materials in the second-level dataset based on our HTC framework to obtain the local database, we develop interpretable supervised classification models to predict ultralow κ_L for efficiently by-passing the complex *ab initio* calculations, which can further refine the results of unsupervised learning and provide greater robustness. Here, materials with κ_{PET} not exceeding 2 W/mK are labeled as 1, which are considered to possess ultralow κ_L ; otherwise, they are labeled as 0, signifying non-ultralow κ_L .

Beyond the input dataset itself, identifying the most relevant features and appropriate algorithms can significantly enhance the generalization and accuracy of ML models, which are also quite strongly intertwined. The chemical compositions and crystal structures of these compounds are also featurized into 273 descriptors based on the aforementioned Magpie data and Voronoi tessellations. As for the ML models, we compare eight widely-used classification algorithms for predicting material properties according to the indica-

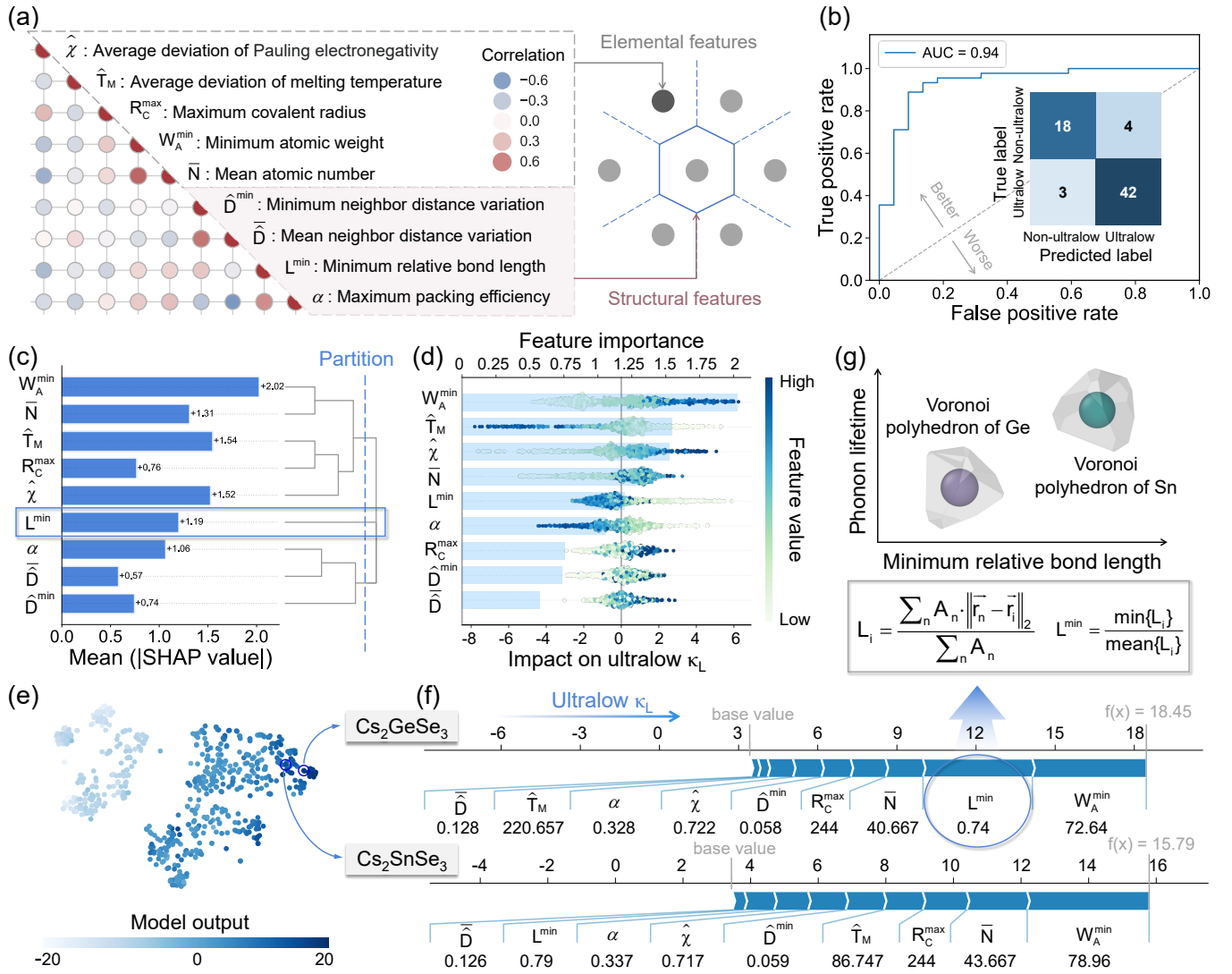


Figure 6. (a–g) Supervised learning based on the local database and interpretable analysis. (a) Heat map of the Pearson correlation coefficient matrix among the selected descriptors and their definitions, which are classified into elemental and structural features. (b) ROC curve and confusion matrix of the optimal ML classification model for predicting ultralow/non-ultralow κ_L . (c) Hierarchical clustering of the descriptors based on their SHAP values. (d) Global interpretability into κ_L classification using SHAP, including the feature importance and the impact of different features on ultralow κ_L . (e) Using t-SNE visualization for the overall contributions of all descriptors of each material to the model output based on their SHAP values. (f) Local interpretability into κ_L classification using SHAP, including the force plots of Cs_2GeSe_3 and Cs_2SnSe_3 . (g) Discovered special descriptor L^{\min} and its trend in influencing the phonon lifetime of Cs_2GeSe_3 and Cs_2SnSe_3 .

tors of Area Under the Receiver Operating Characteristic Curve (ROC AUC) and accuracy based on stratified ten-fold cross-validation (Figure S6): Decision Tree (DT), Extra Trees (ET), Random Forest (RF), Gradient Boosting Classifier (GBC), Adaptive Boosting (AdaBoost), eXtreme Gradient Boosting (XGBoost), Light Gradient Boosting Machine (LightGBM), Categorical Boosting (CatBoost). Most algorithms demonstrate good performances, with the CatBoost algorithm achieving the best results, which is chosen to build the follow-up classification model. To avoid the curse of dimensionality, we perform feature selection using the model-based wrapper method and Pearson correlation method. De-

scriptors are iteratively removed based on the feature importance scores obtained from the CatBoost algorithm, and an ML model is subsequently trained using the remaining descriptors at each step. This process yields the curve depicting the model performance as a function of the number of features (Figure S7), indicating that optimal performance is achieved when utilizing the top 11 features. To reduce the correlation between features, the Pearson correlation coefficients (ρ) of these 11 features are calculated, which are defined as: $\rho = \text{cov}(x_i, x_j) / \sigma_{x_i} \sigma_{x_j}$, where $\text{cov}(x_i, x_j)$ is the covariance of features x_i and x_j , σ_{x_i} is the standard deviation of the feature x_i . For pairs of features with $|\rho| > 0.8$, we

retain the one with the higher feature importance score. [Figure 6a](#) displays the heatmap of the Pearson correlation coefficient matrix among the selected nine features and illustrates the specific meanings of these features based on elemental attributes and Wigner-Seitz cells, indicating that we have successfully eliminated redundant descriptors. We adjust the hyperparameters of the ML model based on Bayesian optimization over 200 random trials, obtaining the best hyperparameters as listed in [Table S3](#). As a result, the performances of the optimal ML classification model is characterized by the ROC curve and the confusion matrix ([Figure 5b](#)), showing its great ability in classifying semiconductors with ultralow κ_L due to the high ROC AUC (0.94), accuracy (0.90), precision (0.90), recall (0.90) and F-score (0.90).

To establish the bridge between descriptors and thermal transport mechanisms thereby demystifying the black-box nature of ML, we perform interpretable analysis for the pre-trained κ_L classification model based on the SHAP method.[\[45, 46\]](#) [Figure 6c](#) shows the dendrogram of the optimal nine descriptors via using the hierarchical clustering based on their SHAP values, where a partition line classifies these features into three groups. Interestingly, beyond the minimum relative bond length L^{\min} , two classes of descriptors based on chemical compositions and crystal structures are identified as we expected. This indicates that L^{\min} may possess a unique influence on ultralow κ_L .

The feature importance and the impact of different features on ultralow κ_L are shown in [Figure 6d](#), which make a global interpretation for the classification model. We here take the most important feature in the three classes as an example to detailedly explain the corresponding hierarchical influence on κ_L combining the SHAP values. For the most important feature W_A^{\min} , defined as:

$$W_A^{\min} = \min\{W_A^1, \dots, W_A^i, \dots, W_A^n\} \quad (1)$$

Where W_A^i is the atomic weight of element i and n is the number of elements, respectively. Semiconductors with larger W_A^{\min} values tend to exhibit low κ_L since the corresponding positive SHAP values, whereas those with smaller W_A^{\min} values show the opposite trend. This can be explained by the dispersion relation for the frequency, just as $\omega = 2\sqrt{\beta/M} |\sin qa/2|$ in a one-dimensional crystal lattice, where β and M are the bond force constant and the atomic mass, respectively. Large M (W) can reduce the frequency ω and thus the group velocity v , resulting in a low κ_L . For the feature α , defined as:

$$\alpha = \frac{NV_{\max}}{V} \times 100 \quad (2)$$

Where N is the number of atoms, V_{\max} is the largest sphere volume occupied by one atom that can fit inside its Voronoi cell, V is the cell volume. It is obvious that low α tends to have a positive effect on ultralow κ_L since its positive SHAP values, which can be explained by its direct effect on the bond length. α helps in understanding how closely the atoms are bonded, with lower values often signifying larger void space with longer bond lengths in a crystal structure. Longer

bond lengths typically result in softer lattices characterized by lower group velocity v , thereby reducing κ_L . As for the special feature L^{\min} , defined as:

$$L^{\min} = \frac{\min\{L_i\}}{\text{mean}\{L_i\}} \quad (3)$$

Where L_i is the weighted average bond length of atom i in a crystal structure, defined as:

$$L_i = \frac{\sum_n A_n \cdot \|\vec{r}_n - \vec{r}_i\|_2}{\sum_n A_n} \quad (4)$$

Where \vec{r}_i is the position of atom i , \vec{r}_n and A_n is the position and the area of the n^{th} neighbor of atom i , respectively. L_i provides a comprehensive description of the interactions between each atom and its nearest neighboring atoms in the crystal structure, with the result influenced by two components: the distance term $\|\vec{r}_n - \vec{r}_i\|_2$ and the weighted term A_n . The distance term $\|\vec{r}_n - \vec{r}_i\|_2$ directly governs the bond length between the nearest neighboring atoms, with shorter distances implying stronger bonding, thus leading to a lower L_i . The weighted term A_n assigns varying weights to different nearest neighboring atoms, where the bond lengths corresponding to the nearest neighboring atoms with greater weights show a higher effect on L_i . Therefore, $\min\{L_i\}$ captures the local information within the structure, which may correspond to covalent bonds due to their typical shorter bond lengths. In contrast, $\text{mean}\{L_i\}$ captures the global information, encompassing both short covalent bonds, long ionic bonds, etc. We propose that the ratio of these two terms, i.e., L^{\min} , might potentially reflect the anharmonicity of materials. Lower L^{\min} values exhibit positive SHAP values, which favor the emergence of ultralow κ_L . This implies that when a structure features lower $\min\{L_i\}$ and higher $\text{mean}\{L_i\}$, it may possess rigidly distorted and weakly bound units with a significant bonding hierarchy, typically leading to stronger anharmonicity, as previously analyzed.

The overall contributions of all descriptors of each material to the model output based on their SHAP values are visualized by the t-SNE method ([Figure 6e](#)), showing that ultralow κ_L (dark blue) and non-ultralow κ_L (light blue) are clearly clustered into the corresponding groups. Cs_2GeSe_3 and Cs_2SnSe_3 are then marked out together to reveal the local interpretability using the SHAP force plots ([Figure 6f](#)), thereby exploring their previously discussed unusual difference of κ_L . Among the features that have the most significant impact on these two materials, L^{\min} surprisingly reaches a level of importance in Cs_2GeSe_3 comparable to that of W_A^{\min} . Although W_A^{\min} in Cs_2GeSe_3 is lower than in Cs_2SnSe_3 , the crucial role of L^{\min} in anharmonicity drives the predicted κ_L of Cs_2GeSe_3 to be much lower. Given the significant difference in phonon lifetime τ between these two materials, as indicated by previous phonon thermal transport analysis, we speculate that L^{\min} might have a great influence on τ , which can be supported by two perspectives. On the one hand, the trend between L^{\min} and τ in Cs_2GeSe_3 and Cs_2SnSe_3 indicates that the former not only exhibits a lower L^{\min} but also has a significantly shorter τ ([Figure 6g](#)). This aligns with the impact

of L^{\min} on anharmonicity revealed by the SHAP analysis. On the other hand, Table S4 indicates that the $\min\{L_i\}$ values in Cs_2GeSe_3 and Cs_2SnSe_3 correspond to the L values derived from the Voronoi polyhedra centered on Ge and Sn, respectively. Although Cs_2GeSe_3 has a lower mean $\{L_i\}$ compared to Cs_2SnSe_3 , its much lower $\min\{L_i\}$ (i.e., L_{Ge}) eventually results in a much lower L^{\min} . This is consistent with the results based on first-principles analysis, which attributes the difference in phonon lifetime to the stronger bond strength (shorter bond length) of Ge–Se covalent bonding compared to that of Sn–Se.

III. CONCLUSION

In summary, we propose a novel HiBoFL framework via integrating unsupervised learning and supervised learning to efficiently predict complex properties and uncover structure-property relationships. As a compelling demonstration, this framework has been applied to efficiently identify semiconductors with ultralow κ_{L} , which circumvents large-scale brute-force DFT calculations without clear objectives. By employing unsupervised learning for the materials from the MP database, we successfully group them into seven clusters. A few hundred materials in clusters C_1 and C_2 with a high likelihood of possessing low κ_{L} is selected from a pool of hundreds of thousands based on similarity design rules. We further conduct low-cost HTC on materials belonging to the two clusters, establishing a local database for researchers to retrieve and providing a list of candidate materials with potential applications in the TE field. Additionally, statistical analysis of these candidates offers valuable domain knowledge to guide the design of materials with ultralow κ_{L} . Cs_2GeSe_3 and Cs_2SnSe_3 with ultralow κ_{L} (~ 0.25 W/mK) are screened out, in which the anomalous ultralow κ_{L} of Cs_2GeSe_3 is attributed to the lower τ caused by the difference in covalent bonding. Based on the established local database, we train a robust ML classification model to refine unsupervised learning, achieving a ROC AUC of 0.94 on the test set, which can enable the efficient predictions of ultralow κ_{L} materials. The interpretable analysis of the classification model reveals the mechanisms of key descriptors on κ_{L} modulation, such as W_{A}^{\min} , α and L^{\min} , etc. The special factor L^{\min} is discovered to show a unique influence on structural anharmonicity, leading to the difference of phonon lifetime in Cs_2GeSe_3 and Cs_2SnSe_3 , in agreement with the first-principles analysis. We believe that this work provides a novel feasible way for efficiently seeking promising TE materials, in which the proposed HiBoFL framework is also expected to be applied in other material fields.

IV. METHODS

A. First-Principles Calculations

All the involved DFT-based first-principles calculations were carried out by using the projector-augmented wave (PAW) method[74] to deal with ion-electron interactions as

implemented in the Vienna *Ab initio* Simulation Package (VASP).[75] in which the processing of data was conducted using VASPKIT.[76] The electronic exchange-correlation energy was described by the Perdew–Burke–Ernzerhof (PBE) functional under the generalized gradient approximation (GGA).[77] Our automatic HTC workflow conducted on the candidate structures identified by unsupervised learning was accomplished within the framework of Python Materials Genomics (Pymatgen).[78] With a plane-wave kinetic energy cutoff of 520 eV and a Γ -centered k -point grid of $2\pi \times 0.04 \text{ \AA}^{-1}$ to sample the Brillouin zone, the structure optimization was terminated when the total energy convergence reached below 10^{-6} eV and the norms of all the forces were less than 0.01 eV/Å. The elastic properties of each material were calculated by applying a 1% change to the volume of the optimized conventional cell. To evaluate the dynamic stability and extract the second-order interaction-force constants (2nd-order IFCs) of Cs_2SnSe_3 and Cs_2GeSe_3 , we used the finite displacement method[79] for calculations as implemented in the Phonopy package.[80, 81] The obtained 2nd-order IFCs were utilized to construct the dynamic matrix and compute the corresponding harmonic properties. Additionally, we utilized the script `thirdorder.py`[82] to generate the $2 \times 2 \times 1$ and $2 \times 2 \times 1$ supercells in consideration of the 10th nearest neighbors for Cs_2SnSe_3 and Cs_2GeSe_3 , thereby resulting in 1504 and 1500 supercells with displaced atoms for self-consistent calculations, respectively. The third-order interaction force constants (3rd-order IFCs) were further extracted to obtain the three-phonon scattering matrix elements, facilitating the calculation of anharmonic properties. Ultimately, we obtained the convergent κ_{L} values of these selected materials as implemented in the ShengBTE package[83] within a $20 \times 20 \times 20$ q -point grid in reciprocal space. The crystal structures and ELF diagrams were visualized using the Crystal Toolkit[84] and VESTA.[85] Moreover, we calculated the COHP as implemented in the LOBSTER code[73] to identify the bonding characteristics as bonding, antibonding or nonbonding.

B. Theoretical Framework

Taking into account the extremely high cost of precisely calculating κ_{L} , we employed the PET model proposed in our previous work[43] within the HTC framework to obtain the corresponding values at 300 K for materials identified by unsupervised learning. The PET model has established the relationship between intrinsic κ_{L} and elastic properties, considering both acoustic phonon and optical phonon contributions, which achieves a certain balance between accuracy and efficiency. The empirical equation of κ_{PET} based on the PET model is expressed as:

$$\kappa_{\text{PET}} = \frac{(6\pi^2)^{2/3}}{3\pi^3} \cdot \frac{\bar{M}}{T(\bar{V}N)^{2/3}} \frac{\bar{v}^3}{\bar{\gamma}^2} + \frac{3k_{\text{B}}\bar{v}}{2\bar{V}^{2/3}} \left(\frac{\pi}{6}\right)^{1/3} (1 - N^{-2/3}) \quad (5)$$

Where \bar{M} is the average atomic mass, T is the temperature, \bar{V} is the average atomic volume, N is the number of atoms in

the primitive cell, k_B is the Boltzmann constant, \bar{v} and $\bar{\gamma}$ are the average sound velocity and average Grüneisen parameter, respectively. Among them, we can obtain \bar{v} as given by:

$$\begin{aligned}\bar{v} &= \left[\frac{1}{3} (\bar{v}_l^{-1} + 2\bar{v}_t^{-3}) \right]^{-1/3} \\ &= \left\{ \frac{1}{3} \left(\frac{\bar{M}}{\bar{V}} \right)^{3/2} \left[\left(B + \frac{4}{3}G \right)^{-3/2} + 2G^{-3/2} \right] \right\}^{-1/3}\end{aligned}\quad (6)$$

And $\bar{\gamma}$ can be expressed as:

$$\begin{aligned}\bar{\gamma} &= \sqrt{\frac{1}{3} (\bar{\gamma}_l^2 + 2\bar{\gamma}_t^2)} \\ &= \sqrt{\frac{1}{3} \left\{ \left[\frac{1}{2} \frac{\partial \ln \left(B + \frac{4}{3}G \right)}{\partial \ln V} + \frac{1}{6} \right]^2 + 2 \left(\frac{1}{2} \frac{\partial \ln G}{\partial \ln V} + \frac{1}{6} \right)^2 \right\}}\end{aligned}\quad (7)$$

Where \bar{v}_l , \bar{v}_t , $\bar{\gamma}_l$ and $\bar{\gamma}_t$ are the longitudinal sound velocity, transverse sound velocity, longitudinal Grüneisen parameter and transverse Grüneisen parameter, respectively. B and G are bulk moduli and shear moduli, respectively. In this manner, we can calculate the κ_{PET} for different materials derived from their elastic properties within the HTC framework. To further validate the κ_{PET} from the PET empirical equation, we calcu-

lated more accurate κ_L values for Cs_2SnSe_3 and Cs_2SnS_3 by solving the phonon Boltzmann transport equation.

C. Machine Learning Toolkit

The chemical compositions and crystal structures were featured into different descriptors using the Matminer package.[86] All parts related to ML were carried out using the Scikit-learn package.[87] To achieve the automation and acceleration of hyperparameter optimization in supervised learning, we employed the powerful Optuna package[88] for efficiently finding the best hyperparameters. And to provide the interpretable analysis of the black-box ML model, a game theoretic approach as implemented in the SHAP package[45, 46] was employed.

ACKNOWLEDGMENTS

We acknowledge the support from the National Natural Science Foundation of China (No. 11935010), the National Key R&D Program of China (No. 2023YFA1406900 and No. 2022YFA1404400), the Natural Science Foundation of Shanghai (No. 23ZR1481200), the Program of Shanghai Academic Research Leader (No. 23XD1423800), and the Opening Project of Shanghai Key Laboratory of Special Artificial Microstructure Materials and Technology.

-
- [1] T. Mueller, A. G. Kusne, and R. Ramprasad, *Rev. Comput. Chem.* **29**, 186 (2016).
- [2] K. Choudhary, B. DeCost, C. Chen, A. Jain, F. Tavazza, R. Cohn, C. W. Park, A. Choudhary, A. Agrawal, S. J. Billinge, *et al.*, *NPJ Comput. Mater.* **8**, 59 (2022).
- [3] Y. Luo, M. Li, H. Yuan, H. Liu, and Y. Fang, *NPJ Comput. Mater.* **9**, 4 (2023).
- [4] Z. Chen, F. C. Bononi, C. A. Sievers, W.-Y. Kong, and D. Donadio, *J. Chem. Theory Comput.* **18**, 4891 (2022).
- [5] V. L. Deringer, M. A. Caro, and G. Csányi, *Adv. Mater.* **31**, 1902765 (2019).
- [6] Z. Yao, B. Sánchez-Lengeling, N. S. Bobbitt, B. J. Bucior, S. G. H. Kumar, S. P. Collins, T. Burns, T. K. Woo, O. K. Farha, R. Q. Snurr, *et al.*, *Nat. Mach. Intell.* **3**, 76 (2021).
- [7] M. Wu, E. Tikhonov, A. Tudi, I. Kruglov, X. Hou, C. Xie, S. Pan, and Z. Yang, *Adv. Mater.* **35**, 2300848 (2023).
- [8] X. Wang, G. Shu, G. Zhu, J.-S. Wang, J. Sun, X. Ding, B. Li, and Z. Gao, *Mater. Today Phys.* **48**, 101549 (2024).
- [9] A. Jain, S. P. Ong, G. Hautier, W. Chen, W. D. Richards, S. Dacek, S. Cholia, D. Gunter, D. Skinner, G. Ceder, *et al.*, *APL Mater.* **1** (2013).
- [10] J. E. Saal, S. Kirklin, M. Aykol, B. Meredig, and C. Wolverton, *Jom* **65**, 1501 (2013).
- [11] S. Kirklin, J. E. Saal, B. Meredig, A. Thompson, J. W. Doak, M. Aykol, S. Rühl, and C. Wolverton, *NPJ Comput. Mater.* **1**, 1 (2015).
- [12] S. Curtarolo, W. Setyawan, G. L. Hart, M. Jahnatek, R. V. Chepul'skii, R. H. Taylor, S. Wang, J. Xue, K. Yang, O. Levy, *et al.*, *Comput. Mater. Sci.* **58**, 218 (2012).
- [13] K. Choudhary, K. F. Garrity, A. C. Reid, B. DeCost, A. J. Baccchi, A. R. Hight Walker, Z. Trautt, J. Hattrick-Simpers, A. G. Kusne, A. Centrone, *et al.*, *NPJ Comput. Mater.* **6**, 173 (2020).
- [14] A. Stuke, M. Todorović, M. Rupp, C. Kunkel, K. Ghosh, L. Himanen, and P. Rinke, *J. Chem. Phys.* **150** (2019).
- [15] K. Takahashi and L. Takahashi, *J. Phys. Chem. Lett.* **10**, 283 (2019).
- [16] A. O. Oliynyk, L. A. Adutwum, J. J. Harynuk, and A. Mar, *Chem. Mater.* **28**, 6672 (2016).
- [17] S. B. Torrisi, M. R. Carbone, B. A. Rohr, J. H. Montoya, Y. Ha, J. Yano, S. K. Suram, and L. Hung, *NPJ Comput. Mater.* **6**, 109 (2020).
- [18] Q. Ren, D. Chen, L. Rao, Y. Lun, G. Tang, and J. Hong, *J. Mater. Chem. A* **12**, 1157 (2024).
- [19] N. Bharadwaj, S. S. Manna, M. K. Jena, D. Roy, and B. Pathak, *J. Mater. Chem. A* (2024).
- [20] M. Xu, Y. Ji, Y. Qin, H. Dong, and Y. Li, *J. Mater. Chem. A* (2024).
- [21] X. Zhang, K. Gu, W. Zhang, J. He, and R. Yang, *ACS Appl. Mater. Interfaces* **16**, 36832 (2024).
- [22] X. Zou, G. Xu, P. Fang, W. Li, Z. Jin, S. Guo, Y. Hu, M. Li, J. Pan, Z. Sun, *et al.*, *Angew. Chem. Int. Ed.* **135**, e202300388 (2023).
- [23] X. Jia, Y. Deng, X. Bao, H. Yao, S. Li, Z. Li, C. Chen, X. Wang, J. Mao, F. Cao, *et al.*, *NPJ Comput. Mater.* **8**, 34 (2022).
- [24] Z. Wang, J. Cai, Q. Wang, S. Wu, and J. Li, *NPJ Comput. Mater.* **7**, 128 (2021).
- [25] J. R. Sootsman, D. Y. Chung, and M. G. Kanatzidis, *Angew. Chem. Int. Ed.* **48**, 8616 (2009).

- [26] G. Pernot, M. Stoffel, I. Savic, F. Pezzoli, P. Chen, G. Savelli, A. Jacquot, J. Schumann, U. Denker, I. Mönch, *et al.*, *Nat. Mater.* **9**, 491 (2010).
- [27] N. P. Padture, M. Gell, and E. H. Jordan, *Science* **296**, 280 (2002).
- [28] Z. Gao, F. Tao, and J. Ren, *Nanoscale* **10**, 12997 (2018).
- [29] Y. Wang and J. Ren, *ACS Appl. Mater. Interfaces* **13**, 34724 (2021).
- [30] C. Xiang, C.-W. Wu, W.-X. Zhou, G. Xie, and G. Zhang, *Front. Phys.* **17**, 1 (2022).
- [31] G. J. Snyder and E. S. Toberer, *Nat. Mater.* **7**, 105 (2008).
- [32] G. Nolas, D. Morelli, and T. M. Tritt, *Annu. Rev. Mater. Sci.* **29**, 89 (1999).
- [33] G. J. Snyder, M. Christensen, E. Nishibori, T. Caillat, and B. B. Iversen, *Nat. Mater.* **3**, 458 (2004).
- [34] S. Mukhopadhyay, D. S. Parker, B. C. Sales, A. A. Puretzky, M. A. McGuire, and L. Lindsay, *Science* **360**, 1455 (2018).
- [35] M. K. Jana, K. Pal, A. Warankar, P. Mandal, U. V. Waghmare, and K. Biswas, *J. Am. Chem. Soc.* **139**, 4350 (2017).
- [36] M. K. Jana, K. Pal, U. V. Waghmare, and K. Biswas, *Angew. Chem. Int. Ed.* **55**, 7792 (2016).
- [37] H. Lin, G. Tan, J.-N. Shen, S. Hao, L.-M. Wu, N. Calta, C. Malliakas, S. Wang, C. Uher, C. Wolverton, *et al.*, *Angew. Chem. Int. Ed.* **55**, 11431 (2016).
- [38] M. D. Nielsen, V. Ozolins, and J. P. Heremans, *Energy Environ. Sci.* **6**, 570 (2013).
- [39] L. Ward, A. Agrawal, A. Choudhary, and C. Wolverton, *NPJ Comput. Mater.* **2**, 1 (2016).
- [40] L. Ward, R. Liu, A. Krishna, V. I. Hegde, A. Agrawal, A. Choudhary, and C. Wolverton, *Phys. Rev. B* **96**, 024104 (2017).
- [41] H. Abdi and L. J. Williams, *Wiley Interdiscip. Rev. Comput. Stat.* **2**, 433 (2010).
- [42] L. Van der Maaten and G. Hinton, *J. Mach. Learn. Res.* **9** (2008).
- [43] S. Yan, Y. Wang, F. Tao, and J. Ren, *J. Phys. Chem. A* **126**, 8771 (2022).
- [44] L. Prokhorenkova, G. Gusev, A. Vorobev, A. V. Dorogush, and A. Gulin, *Advances in neural information processing systems* **31** (2018).
- [45] L. S. Shapley, *Contributions to the Theory of Games II*, *Annals of Mathematical Studies* **28**, 307 (1953).
- [46] S. Lundberg, S. Lee, I. Guyon, U. Luxburg, and S. Bengio, *Adv. Neural Inf. Process. Syst.* **30**, 4768 (2017).
- [47] M. Cui *et al.*, *Accounting, Auditing and Finance* **1**, 5 (2020).
- [48] K. R. Shahapure and C. Nicholas, in *2020 IEEE 7th international conference on data science and advanced analytics (DSAA)* (IEEE, 2020) pp. 747–748.
- [49] M. D. Ewbank, P. R. Newman, and H. Kuwamoto, *J. Appl. Phys.* **53**, 6450 (1982).
- [50] D. Spitzer, *J. Phys. Chem. Solids* **31**, 19 (1970).
- [51] E. J. Skoug and D. T. Morelli, *Phys. Rev. Lett.* **107**, 235901 (2011).
- [52] N. Popovich and V. Shura, *J. Phys.: Condens. Matter* **15**, 5389 (2003).
- [53] W. M. Haynes, *CRC handbook of chemistry and physics* (CRC press, 2016).
- [54] J. D. Beasley, *Appl. Opt.* **33**, 1000 (1994).
- [55] G. A. Slack, R. A. Tanzilli, R. Pohl, and J. Vandersande, *J. Phys. Chem. Solids* **48**, 641 (1987).
- [56] D. T. Morelli and G. A. Slack, in *High thermal conductivity materials* (Springer, 2006) pp. 37–68.
- [57] G. A. Slack, *J. Phys. Chem. Solids* **34**, 321 (1973).
- [58] S. L. Shindé and J. Goela, *High thermal conductivity materials*, Vol. 91 (Springer, 2006).
- [59] C. J. Glassbrenner and G. A. Slack, *Phys. Rev.* **134**, A1058 (1964).
- [60] MongoDB. <https://www.mongodb.com/>.
- [61] Y. Cao, S. Dai, X. Wang, T. Wei, J. Yang, L. Xi, Z. Pang, and G. Tan, *Appl. Phys. Lett.* **124** (2024).
- [62] R. Li, X. Li, L. Xi, J. Yang, D. J. Singh, and W. Zhang, *ACS Appl. Mater. Interfaces* **11**, 24859 (2019).
- [63] S. K. Guillemot, A. Suwardi, N. Kaltsoyannis, and J. M. Skelton, *J. Mater. Chem. A* **12**, 2932 (2024).
- [64] T. Deng, J. Recatala-Gomez, M. Ohnishi, D. M. Repaka, P. Kumar, A. Suwardi, A. Abutaha, I. Nandhakumar, K. Biswas, M. B. Sullivan, *et al.*, *Materials Horizons* **8**, 2463 (2021).
- [65] J. J. Plata, V. Posligua, A. M. Márquez, J. Fernandez Sanz, and R. Grau-Crespo, *Chem. Mater.* **34**, 2833 (2022).
- [66] V. Posligua, J. J. Plata, A. M. Márquez, J. F. Sanz, and R. Grau-Crespo, *ACS Applied Electronic Materials* **6**, 2951 (2023).
- [67] Y. Pei, X. Shi, A. LaLonde, H. Wang, L. Chen, and G. J. Snyder, *Nature* **473**, 66 (2011).
- [68] J. P. Heremans, *Nat. Phys.* **11**, 990 (2015).
- [69] X. Zeng, J. Jiang, G. Niu, L. Sui, Y. Zhang, X. Wang, X. Liu, A. Chen, M. Jin, and K. Yuan, *J. Phys. Chem. Lett.* **13**, 9736 (2022).
- [70] C. Chang and L.-D. Zhao, *Mater. Today Phys.* **4**, 50 (2018).
- [71] J. Li, W. Hu, and J. Yang, *J. Am. Chem. Soc.* **144**, 4448 (2022).
- [72] S. Kawano, T. Tadano, and S. Iikubo, *J. Phys. Chem. C* **125**, 91 (2021).
- [73] R. Dronskowski and P. E. Blöchl, *J. Phys. Chem.* **97**, 8617 (1993).
- [74] G. Kresse and D. Joubert, *Phys. Rev. B* **59**, 1758 (1999).
- [75] G. Kresse and J. Furthmüller, *Phys. Rev. B* **54**, 11169 (1996).
- [76] V. Wang, N. Xu, J.-C. Liu, G. Tang, and W.-T. Geng, *Comput. Phys. Commun.* **267**, 108033 (2021).
- [77] J. P. Perdew, K. Burke, and M. Ernzerhof, *Phys. Rev. Lett.* **77**, 3865 (1996).
- [78] S. P. Ong, W. D. Richards, A. Jain, G. Hautier, M. Kocher, S. Cholia, D. Gunter, V. L. Chevrier, K. A. Persson, and G. Ceder, *Comput. Mater. Sci.* **68**, 314 (2013).
- [79] S. Baroni, S. De Gironcoli, A. Dal Corso, and P. Giannozzi, *Rev. Mod. Phys.* **73**, 515 (2001).
- [80] A. Togo, L. Chaput, T. Tadano, and I. Tanaka, *J. Phys. Condens. Matter* **35**, 353001 (2023).
- [81] A. Togo, *J. Phys. Soc. Jpn.* **92**, 012001 (2023).
- [82] W. Li, L. Lindsay, D. A. Broido, D. A. Stewart, and N. Mingo, *Phys. Rev. B* **86**, 174307 (2012).
- [83] W. Li, J. Carrete, N. A. Katcho, and N. Mingo, *Comp. Phys. Commun.* **185**, 1747–1758 (2014).
- [84] M. Horton, J.-X. Shen, J. Burns, O. Cohen, F. Chabbey, A. M. Ganose, R. Guha, P. Huck, H. H. Li, M. McDermott, *et al.*, *arXiv preprint arXiv:2302.06147* (2023).
- [85] K. Momma and F. Izumi, *J. Appl. Crystallogr.* **44**, 1272 (2011).
- [86] L. Ward, A. Dunn, A. Faghaninia, N. E. Zimmermann, S. Bajaj, Q. Wang, J. Montoya, J. Chen, K. Bystrom, M. Dylla, *et al.*, *Comput. Mater. Sci.* **152**, 60 (2018).
- [87] F. Pedregosa, G. Varoquaux, A. Gramfort, V. Michel, B. Thirion, O. Grisel, M. Blondel, P. Prettenhofer, R. Weiss, V. Dubourg, *et al.*, *J. Mach. Learn. Res.* **12**, 2825 (2011).
- [88] T. Akiba, S. Sano, T. Yanase, T. Ohta, and M. Koyama, in *Proceedings of the 25th ACM SIGKDD international conference on knowledge discovery & data mining* (2019) pp. 2623–2631.